Imaging Crystals, Polymers, and Processes in Water with the Atomic Force Microscope

Author(s): B. Drake, C. B. Prater, A. L. Weisenhorn, S. A. C. Gould, T. R. Albrecht, C. F. Quate, D. S. Cannell, H. G. Hansma and P. K. Hansma

Source: *Science*, Mar. 24, 1989, New Series, Vol. 243, No. 4898 (Mar. 24, 1989), pp. 1586-1589

Published by: American Association for the Advancement of Science

Stable URL: https://www.jstor.org/stable/1703636

Four of the groups have albedo estimates near the full-experiment average (0.093), but the first group, which covers most of the large crater Stickney and its ejecta blanket, has a lower value, while the fourth, which covers the region antipodal to Stickney, has a higher value. These variations might arise from the different distributions of large-scale (meter-to-kilometer) surface slopes for the sampled orientations of Phobos, or from regional differences in regolith bulk density (Table 2), or both.

How does Phobos's radar signature compare with those of other planetary objects, and in particular with those of C-class asteroids? Figure 2 plots 3.5-cm estimates of (μ_c, $\hat{\sigma}_{oc}$) for the moon (*17–19*) and three small, Earth-approaching objects: the ~1.5-km, C-class asteroid 1986 JK (*20*); the ~20-km, S-class asteroid 433 Eros (*21*); and the ~10-km nucleus of comet IRAS-Araki-Alcock (*22*). A 13-cm point for the ~2-km, C-class, Earth-approaching asteroid 2100 Ra-Shalom (*23*) is also shown. Mainbelt asteroid results are available just at 13 cm (*10*); we show the mean value and rms dispersions of (μ_c, $\hat{\sigma}_{oc}$) for nine large (>100-km), C-class objects and individual estimates for the two largest [1 Ceres (~930 km) and 2 Pallas (~540 km)], as well as the mean and root-mean-square values of (μ_c, $\hat{\sigma}_{oc}$) for seven large, S-class objects. Experience with objects observed at both wavelengths leads us to expect μ_c ~ 30% to ~ 300% larger at 3.5 cm (*18*, *21*).

In this light, Fig. 2 suggests that Phobos bears a closer resemblance to large, C-class, mainbelt asteroids than to other planetary targets. On the other hand, the moon (*17*) and the small, Earth-approaching bodies have larger μ_c estimates than Phobos, indicating more severe small-scale roughness. This result, as well as the variance in radar albedo (and hence in near-surface bulk density), might reflect intrinsic differences in the physical properties of surface materials or variations in regolith generating processes (*1*).

In summary, Phobos's surface apparently resembles those of many (if not most) large, C-class asteroids in terms of bulk density, small-scale roughness, and large-scale topographic character, but differs from the surfaces of the moon and at least some small, Earth-approaching objects. Additional 3.5-cm and 13-cm radar observations of asteroids, comets, and the martian satellites can clarify these relations.

REFERENCES AND NOTES

1. J. Veverka and J. A. Burns, *Annu. Rev. Earth Planet. Sci.* **8**, 527 (1980).
2. D. J. Stevenson, A. W. Harris, J. I. Lunine, in *Satellites*, J. A. Burns and M. S. Matthews, Eds. (Univ. of Arizona Press, Tucson, 1986), pp. 39–88.
3. J. E. Oberg, *Mission to Mars* (Stackpole Books, Harrisburg, 1982), pp. 149–157.
4. Nominal radar system characteristics were as follows: one-way antenna gain at zenith, $10^{7.2}$; minimum system temperature, 18 K; transmitter power, 350 kW.
5. S. J. Ostro, D. B. Campbell, I. I. Shapiro, *Astron. J.* **88**, 565 (1983).
6. Ellipsoidal approximations to Phobos's figure, tabulated by T. C. Duxbury (*Icarus*, in press), have semi-axis lengths that satisfy: $12.61 \leq a \leq 13.3$, $11.1 \leq b \leq 11.33$, and $8.6 \leq c \leq 9.3$ km.
7. M. J. Campbell and J. Ulrichs, *J. Geophys. Res.* **74**, 5867 (1969).
8. P. Thomas, J. Veverka, S. Dermott, in *Satellites*, J. A. Burns and M. S. Matthews, Eds. (Univ. of Arizona Press, Tucson, 1986), p. 831.
9. R. A. Simpson and G. L. Tyler, *IEEE Trans. Antennas Propag.* **AP-30**, 438 (1982).
10. S. J. Ostro, D. B. Campbell, I. I. Shapiro, *Science* **229**, 442 (1985).
11. The uncertainty assigned to σ_{oc} incorporates statistical error attributable to receiver noise and much larger systematic errors arising primarily from uncertainty in antenna gain and pointing accuracy.
12. J. B. Garvin, J. W. Head, G. H. Pettengill, S. H. Zisk, *J. Geophys. Res.* **90**, 6859 (1985).
13. J. A. Burns, in *Satellites*, J. A. Burns and M. S. Matthews, Eds. (Univ. of Arizona Press, Tucson, 1986), p. 14.
14. K. D. Pang *et al.*, *Science* **199**, 64 (1978).
15. B. P. Glass, *Introduction to Planetary Geology* (Cambridge Univ. Press, Cambridge, 1982), p. 101.
16. W. D. Carrier III, J. K. Mitchell, A. Mahmood, *Proc. Lunar. Sci. Conf.* **4**, 2403 (1973).
17. Our value for the moon's μ_c ($0.33^{+0.14}_{-0.08}$) combines a 3.5-cm OC albedo of 0.07 ± 0.02 (*18*) with a 3.8-cm SC albedo of 0.023 ± 0.003, derived from (*19*). Unlike the other targets in Fig. 2, the moon's OC spectrum has a very sharp central peak caused by powerful back-reflections from the sub-radar region at the center of the visible disk. μ_c decreases sharply away from the disk's center, and values far from the center are thought to be a better indicator of the severity of wavelength-scale roughness than the disk-integrated value [J. K. Harmon and S. J. Ostro, *Icarus* **62**, 110 (1985)]. The outermost 60% of the moon's disk has $\mu_c \geq 0.30$, while $\mu_c \geq 0.60$ near the limb (*19*).
18. G. H. Pettengill, *Annu. Rev. Astron. Astrophys.* **16**, 265 (1978).
19. S. H. Zisk, G. H. Pettengill, G. W. Catuna, *Moon* **10**, 17 (1974), figure 10.
20. S. J. Ostro *et al.*, *Icarus*, in press.
21. R. F. Jurgens and R. M. Goldstein, *ibid.* **28**, 1 (1976); B. Zellner, *ibid.*, p. 149. S-class asteroids are thought to be mineralogically similar to stony-iron or ordinary chondritic meteorites.
22. R. M. Goldstein, R. F. Jurgens, Z. Sekanina, *Astron. J.* **89**, 1745 (1984); Z. Sekanina, *ibid.* **95**, 1876 (1988).
23. S. J. Ostro, A. W. Harris, D. B. Campbell, I. I. Shapiro, J. W. Young, *Icarus* **60**, 391 (1984); S. J. Ostro, D. B. Campbell, I. I. Shapiro, *Bull. Amer. Astron. Soc.* **17**, 729 (1985). Most 13-cm values of μ_c for small, non–C-class, Earth-approaching objects range from 0.2 to 1.0.

24. We thank D. Choate, P. Dendrenos, C. Ellston, R. Genzmer, L. Robinett, S. Walmer, and R. Winkler for help with the observations. This research was conducted at the Jet Propulsion Laboratory, California Institute of Technology, under contract with the National Aeronautics and Space Administration.

19 January 1989; accepted 24 February 1989

Imaging Crystals, Polymers, and Processes in Water with the Atomic Force Microscope

B. DRAKE, C. B. PRATER, A. L. WEISENHORN, S. A. C. GOULD, T. R. ALBRECHT, C. F. QUATE, D. S. CANNELL, H. G. HANSMA, P. K. HANSMA

The atomic force microscope (AFM) can be used to image the surface of both conductors and nonconductors even if they are covered with water or aqueous solutions. An AFM was used that combines microfabricated cantilevers with a previously described optical lever system to monitor deflection. Images of mica demonstrate that atomic resolution is possible on rigid materials, thus opening the possibility of atomic-scale corrosion experiments on nonconductors. Images of polyalanine, an amino acid polymer, show the potential of the AFM for revealing the structure of molecules important in biology and medicine. Finally, a series of ten images of the polymerization of fibrin, the basic component of blood clots, illustrate the potential of the AFM for revealing subtle details of biological processes as they occur in real time.

THE ATOMIC FORCE MICROSCOPE (AFM) (*1*) gives topographic images by scanning a sharp tip over a surface (*2*) and has been used to produce atomic-resolution images of both conductors (*3*) and nonconductors (*4*). Its published technological applications already include atomic-scale friction measurements (*5*), imaging of magnetic fields above thin-film recording heads (*6*), imaging of polymers (*7*), and imaging of photoresist on silicon (*8*).

The images we present in this report show that the AFM can be used on a large and important class of systems: nonconductors covered with aqueous solutions. This class includes many important systems in biology, medicine, and technology, from mitochondria in cytoplasm to painted ships in seawater. The AFM obtains images fast enough (a few seconds per image) to observe many biological and chemical processes in real time.

A new, gentler and more reliable AFM

B. Drake, C. B. Prater, A. L. Weisenhorn, S. A. C. Gould, D. S. Cannell, H. G. Hansma, P. K. Hansma, Department of Physics, University of California, Santa Barbara, CA 93106.
T. R. Albrecht and C. F. Quate, Department of Applied Physics, Stanford University, Stanford, CA 94305.

(Fig. 1) made it possible to obtain these images. It is gentler because it presses on the surface being imaged with a smaller force than ever before, as low as 2×10^{-9} N. Gentler and more reliable operation was obtained by combining an optical lever (*9*) with microfabricated cantilevers (*10*). The optical lever amplifies the motion of the tip of the cantilever, δz, to produce a motion of the reflected beam at the detector (*11*) that is greater by a factor of $2L/l$, where $L \approx 4$ cm is the distance from the cantilever to the photodiode and $l \approx 100$ μm is the length of the cantilever. This factor of 800 is sufficient so that we are not limited by the photodiode sensitivity but rather by sound and building vibrations. The effective noise level δz is approximately 0.02 nm root-mean-square in the frequency range from 0.1 to 20 kHz. This noise level is low enough to permit routine atomic-resolution imaging. The rest of the AFM is similar to microscopes we have described previously (see, for example, figure 2B in (*2*)]. The mechanical approach of the sample to the cantilever is done with two fine screws that are turned by hand and one that is driven with a stepper motor. The sample is then scanned with a single-tube *xyz* piezoelectric translator with a range of 0.45 μm.

Operating the AFM with the cantilever and sample in water (Fig. 1) allows not only for physiologically more realistic environments, but also for better control of the forces that are applied to the sample. Surfaces in air are typically covered with an adsorbed layer of water and unknown contaminants. When a tip covered with a layer of contaminants comes near a sample that is also covered, there is an adhesion force that drives the tip towards the sample (*12, 13*). This force can be much larger than the applied forces we want to use. A typical value is 10^{-7} N (*12*). Operation with water eliminates this undesirable and often destructive force since the tip and cantilever are always completely covered with fluid. Thus operation in water (or other fluids) allows the applied force to be more precisely known and controlled. Furthermore, there is no problem in switching to concentrated aqueous solutions. For example, we have operated the AFM with seawater on stainless steel and aluminum in preliminary corrosion experiments.

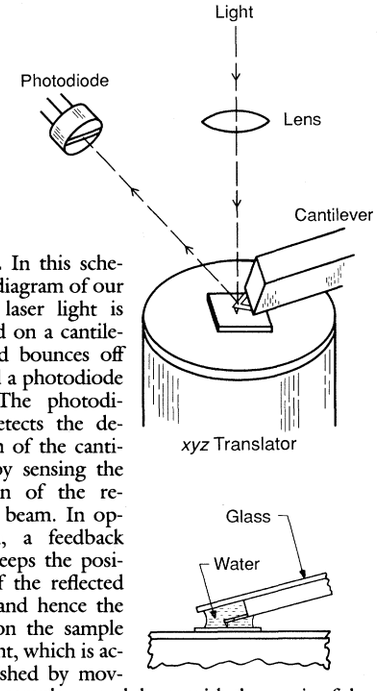

Fig. 1. In this schematic diagram of our AFM, laser light is focused on a cantilever and bounces off toward a photodiode (*11*). The photodiode detects the deflection of the cantilever by sensing the position of the reflected beam. In operation, a feedback loop keeps the position of the reflected beam and hence the force on the sample constant, which is accomplished by moving the sample up and down with the *z*-axis of the piezoelectric translator as the sample is scanned underneath it with the *x*- and *y*-axes. An optional small cell formed by the sample and a microscope cover glass can be filled with water to image samples in water.

This new microscope is much better than our earlier models (*14*), which used electron tunneling to measure the deflection of the cantilever. Imaging under water, together with the use of light to detect the deflection of the cantilever, eliminates the large, unknown forces and erratic operation common to our tunneling AFMs.

The lateral resolution of this new AFM for samples in aqueous solutions can be better than 0.5 nm. For example, mica cleaves along flat planes of atoms that can be revealed by the AFM (Fig. 2A). The nearly hexagonal array of dark spots in the image corresponds to holes in the center of hexagonal rings of atoms in these flat planes (*15*). The holes in these rings are separated by approximately 5.2 Å. Holes separated by 2.46 Å were observed on graphite under water. We choose to present the mica image because (i) it has been an important test surface for studying intramolecular and surface forces (*13*) and (ii) the aqueous solution over the mica was a solution of protein in buffer. Although we could sometimes detect the presence of something the size of a protein, it would usually disappear before a complete image could be obtained. Consequently, we usually saw only the mica. Presumably the protein did not attach well enough to mica to be imaged at the forces we used.

Biological compounds could be imaged if they were allowed to attach to glass surfaces. The amino acid polymer polyalanine (*16*) is shown in Fig. 2, B and C. It was dissolved in 85% chloroform–15% trifluoroacetic acid at a concentration of 40 μg/ml. A drop of the solution was placed on a washed microscope slide, and the excess solution was blown off with filtered compressed air. The slide was then washed with filtered deionized water, which was also blown off with clean compressed air. The sample was then put into the microscope and rehydrated with a drop of water (Fig. 2B). It was also possible to image polyalanine without water (Fig. 2C). In other images taken without water, the atomic lattice of mica, graphite, and DL-leucine were resolved.

The microscope can also image biological and chemical processes. In this report we present images (Fig. 3) taken during the thrombin-catalyzed polymerization of the protein fibrin. Since the polymerization of fibrin is responsible for blood clotting, it is an important model system for demonstrating the potential of the AFM. Fibrinogen (*16*) was dissolved in 50 m*M* sodium phosphate buffer, *p*H 7, containing 0.2 *M* NaCl, and was then filtered. A few drops of solution were placed on a mica substrate. We imaged the surface for a few minutes and saw fleeting images of fibrinogen molecules (Fig. 3A). As mentioned above, the molecules did not adhere well enough to the mica to be reproducible.

We then added a few drops of the clotting enzyme thrombin (2 NIH units per milliliter in water) and continued to image the surface. Thrombin removes a set of peptides from the central region of the fibrinogen molecule, which turns the molecule into a fibrin monomer (*17*). Removal of these peptides unmasks polymerization sites, which allows the molecule to polymerize spontaneously (*18*). As the fibrin monomers polymerized into larger aggregates, they were more reproducibly imaged (Fig. 3B). These aggregates did move, however, growing larger and connecting to each other (Fig. 3, C, D, E, and F) until a single chain spanned our field of view (Fig. 3G). Next, a second chain grew adjacent to the first (Fig. 3H), then a third (Fig. 3I). Finally, 33 min after the addition of thrombin, the field of view was nearly covered with a fibrin net (Fig. 3J). Fibrin nets like these play a vital role in many biological processes, ranging from the healing of wounds to the formation of clots that produce heart attacks and strokes.

In at least one image (Fig. 3D), the three-ball structure known from transmission electron microscopy (*17*) can be seen in a single fibrin monomer that is not yet polymerized into a chain. We have also obtained images of single monomers on glass where the three-ball structure can be seen more clearly. It would be desirable to see substructure comparable to that in Fig. 2, B and C. Although we have observed such structure in a few images, it is not yet reproducible.

We can consider what limits the resolution of imaging proteins. One limitation that may soon be lifted is the lack of light,

well-characterized tips. At present we use shards of a shattered diamond for our tips. The smallest shards that we can handle and glue onto the cantilevers have a mass $m \sim 2 \times 10^{-11}$ kg. This mass dominates the mass of the tip-cantilever system and limits how soft we can make the cantilevers; in order to acquire complete images (256 pixels on each of 512 lines) in times of order 5 s requires a resonant frequency of the tip-cantilever system $\nu \geq 20$ kHz. Thus $k[= m(2\pi\nu)^2]$ must be greater than 1.5 N/m. Microfabricated tips on the cantilevers could have an order of magnitude smaller mass m, thus allowing us to reduce k by an order of magnitude while retaining $\nu \geq 20$ kHz. This design would give us an even gentler AFM that could resolve more subtle and fragile structures.

A more fundamental limitation is protein motion in water. This limitation might be minimized by imaging in more viscous fluids, or by lowering the temperature. Proteins could be imaged at temperatures near freezing in water, or, for the ultimate in resolution, to liquid nitrogen temperature or below; AFMs have already been operated in cryogenic fluids (*19*). The new optical lever detection scheme should make operating in cryogenic fluids much easier.

A continuing challenge for the AFM, as for other microscopes, is developing new sample preparation techniques. Fortunately, pioneering work on biological samples (*20*) and thin organic films (*21*) with another scanning probe microscope, the scanning tunneling microscope (*22*), can point to effective techniques for the AFM. For example, techniques have been developed to plate ordered arrays of DNA on flat surfaces (*23*). With the AFM it should be possible to look not only at these samples, but also at thicker, nonconducting samples and at samples on nonconducting substrates.

There are several natural extensions of this work. One is to image short polypeptides, such as some hormones. Furthermore, we hope that within a few years, the AFM provides images of larger proteins with sufficient detail to allow computer simulations to converge on their three-dimensional structure. Finally, since the microscope can image samples under aqueous solutions with sufficient speed for real-time observation, the AFM has the potential to image a whole class of biological and chemical processes.

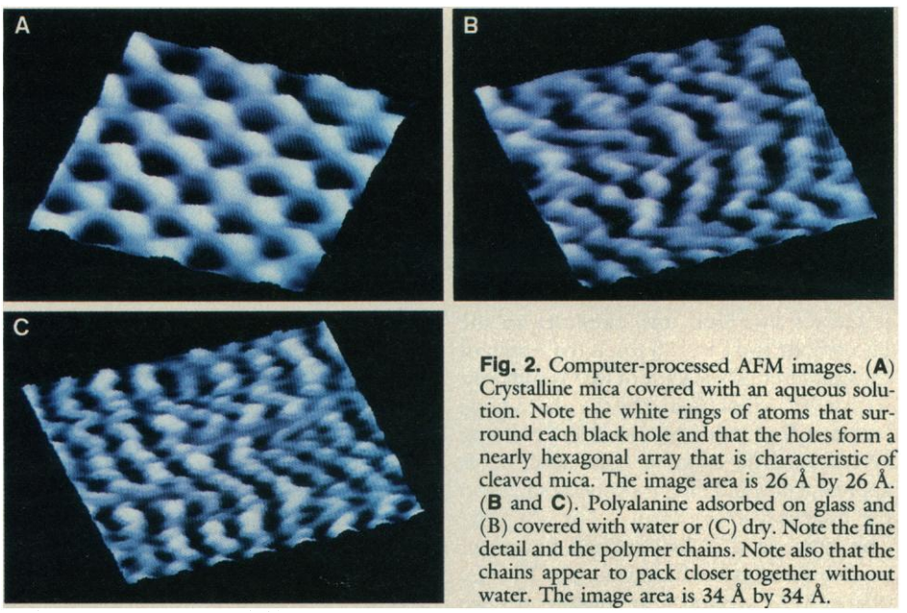

Fig. 2. Computer-processed AFM images. (**A**) Crystalline mica covered with an aqueous solution. Note the white rings of atoms that surround each black hole and that the holes form a nearly hexagonal array that is characteristic of cleaved mica. The image area is 26 Å by 26 Å. (**B** and **C**). Polyalanine adsorbed on glass and (B) covered with water or (C) dry. Note the fine detail and the polymer chains. Note also that the chains appear to pack closer together without water. The image area is 34 Å by 34 Å.

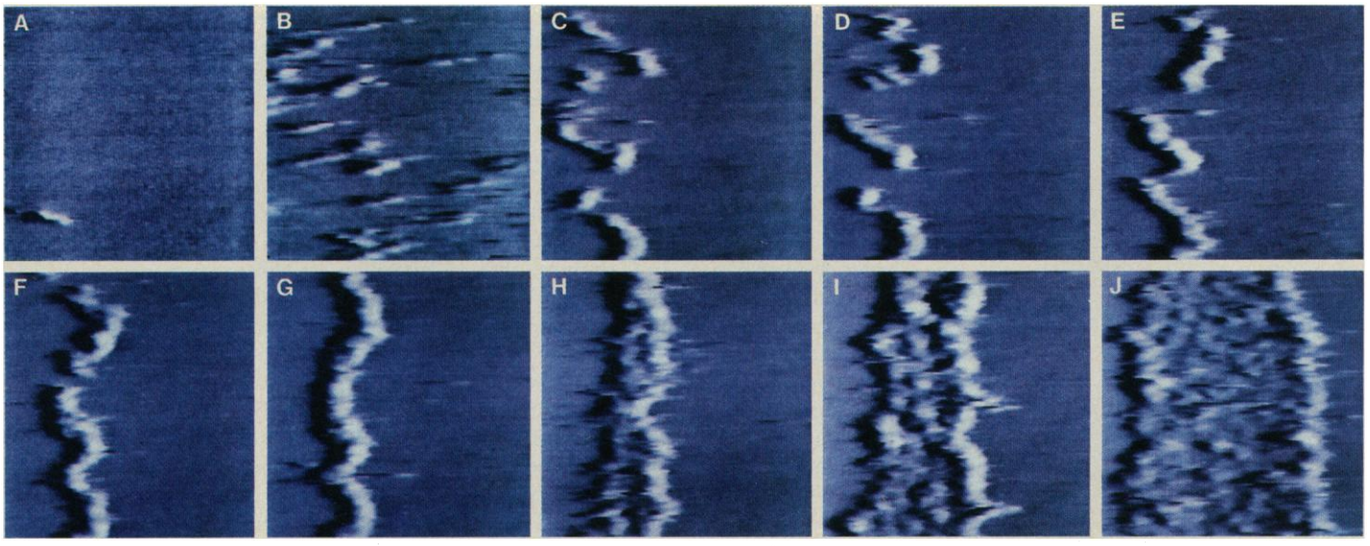

Fig. 3. Ten AFM images from a video cassette recorder tape that show clotting of the human blood protein fibrinogen in real time. The images were selected from before introduction of the clotting enzyme thrombin (**A**), and at various times after its introduction: 9 min (9′), 10 min 20 s (10′20″), 10′30″, 11′20″, 12′10″, 12′40″, 14′50″, 17′10″, 33′ for (**B**) through (**J**). Each image area is 4500 Å by 4500 Å.

REFERENCES AND NOTES

1. G. Binnig, C. F. Quate, Ch. Gerber, *Phys. Rev. Lett.* **56**, 930 (1986).
2. P. K. Hansma *et al.*, *Science* **242**, 209 (1988).
3. G. Binnig *et al.*, *Europhys. Lett.* **3**, 1281 (1987).
4. T. R. Albrecht and C. F. Quate, *J. Appl. Phys.* **62**, 2599 (1987).
5. C. M. Mate, G. M. McClelland, R. Erlandson, S. Chiang, *Phys. Rev. Lett.* **59**, 1942 (1987).
6. Y. Martin and H. K. Wickramasinghe, *Appl. Phys. Lett.* **50**, 1455 (1987).
7. T. R. Albrecht *et al.*, *J. Appl. Phys.* **64**, 1178 (1988).
8. Y. Martin *et al.*, *Scanning Microsc.* **2**, 3 (1988).
9. N. M. Amer and G. Meyer, *Bull. Am. Phys. Soc.* **33**, 319 (1988); G. Meyer and N. M. Amer, *Appl. Phys. Lett.* **53**, 1045 (1988); S. Alexander *et al.*, *J. Appl. Phys.* **65**, 164 (1989).
10. T. R. Albrecht and C. F. Quate, *J. Vac. Sci. Technol.* **A 6**, 271 (1988).
11. Model SPOT-4D from United Detector Technology. We use two segments of this four-segment

photodiode to get lower capacitance than in a two-segment photodiode. We use $(A - B)/(A + B)$ as our deflection signal, where A and B are the signals from the two segments of the photodiode. This signal is independent of laser intensity fluctuations, which are otherwise a significant source of noise.
12. M. Mate helped us understand and estimate this force. His AFM measurements of this force are consistent with the formula given by Israelachvili (*13*, p. 221): $F = 4\pi R\delta_s$ where R is the tip radius ($\approx$0.1 μm) and δ_s is the surface tension of the liquid, 7×10^{-2} N/m for water. Thus $F \approx 10^{-7}$ N.
13. J. N. Israelachvili, *Intermolecular and Surface Forces with Applications to Colloidal and Biological Systems* (Academic Press, New York, 1985).
14. O. Marti, B. Drake, P. K. Hansma, *Appl. Phys. Lett.* **51**, 484 (1987); O. Marti, B. Drake, S. Gould, P. K. Hansma, *J. Vac. Sci. Technol.* **A 6**, 2089 (1988); O. Marti *et al.*, *Science* **239**, 50 (1988); O. Marti, S. Gould, P. K. Hansma, *Rev. Sci. Instrum.* **59**, 836 (1988); S. Gould *et al.*, *Nature* **332**, 332 (1988).
15. The symmetry of the rings is distorted from hexagonal by ~0.5% in our mica, muscovite [W. A. Deer, R. A. Howie, J. Zussman, *An Introduction to the Rock Forming Minerals*, (Longman, London, ed. 8, 1975), pp. 193–205]. Uncertainty due to thermal drift in the effective γ calibration makes observation of such a subtle distortion impossible for now.
16. From Sigma Chemical Co., St. Louis, MO.
17. M. W. Mosesson and R. F. Doolittle, Eds., *Molecular Biology of Fibrinogen and Fibrin*, vol. 408 of *Annals of the New York Academy of Sciences* (New York Academy of Sciences, New York, 1983).
18. R. F. Doolittle, *Annu. Rev. Biochem.* **53**, 195 (1984).
19. M. D. Kirk, T. R. Albrecht, C. F. Quate, *Rev. Sci. Instrum.* **59**, 833 (1988).
20. See, as examples, A. M. Baró *et al.*, *Nature* **315**, 253 (1985); S. M. Lindsay and B. Barris, *J. Vac. Sci. Technol. A* **6**, 544 (1988); D. C. Dahn *et al.*, *ibid.*, p. 548; A. Stemmer *et al.*, *Surf. Sci.* **181**, 394 (1987); G. Travaglini *et al.*, *ibid.*, p. 380; M. Amrein, A. Stasiak, H. Gross, E. Stoll, G. Travaglini, *Science* **240**, 514 (1988); L. Feng, C. Z. Hu, J. D. Andrade, *J. Colloid Interface Sci.* **126**, 650 (1988); A. Stemmer *et al.*, *Ultramicroscopy* **25**, 171 (1988); R. Guckenberger *et al.*, *ibid.*, p. 111. Fibrinogen deposited on graphite has been imaged with an STM operating in air by L. Feng, C. Z. Hu, J. D. Andrade, unpublished results.
21. See, as examples, D. P. E. Smith *et al.*, *Proc. Natl. Acad. Sci. U.S.A.* **84**, 969 (1987); C. A. Lang *et al.*, *J. Vac. Sci. Technol. A* **6**, 368 (1988); J. Foster, J. E. Frommer, P. C. Arnett, *Nature* **331**, 324 (1988); J. B. Pethica, *ibid.*, p. 301; J. S. Foster and J. E. Frommer, *ibid.* **333**, 542 (1988).
22. G. Binnig, H. Rohrer, Ch. Gerber, E. Weibel, *Phys. Rev. Lett.* **49**, 57 (1982).
23. B. Barris *et al.*, *BioPolymers* **27**, 1691 (1988).
24. We thank R. F. Doolittle for suggesting the fibrin polymerization experiment; S. Alexander, M. Wilson, R. Stuber and V. Elings for help with the design of our AFM; C. Bracker, G, Taborsky, S. Parsons, H. K. Wickramasinghe, N. M. Amer, M. Kirk, R. F. Doolittle, C. Singh, D. Case, R. V. Coleman, F. Ohnesorge, S. Manne, O. Marti, M. Mate, R. Barrett, R. Sonnenfeld, G. Dietler, and S. Sutter for their help and useful discussions; W. Stoeckenius and I. Giaver for emphasizing the importance of looking at polypeptides and proteins; D. Nelson for suggesting that we look at corrosion processes; and G. Somorjai for originally making us aware of the importance of studying solid-liquid interfaces. Supported by National Science Foundation–Solid State Physics grant DMR-86-13486 (S.A.C.G., H.G.H., P.K.H., and A.L.W.), Low Temperature Physics grant DMR-88-14485 (D.S.C.), the Office of Naval Research (B.D., P.K.H., and C.B.P.), a National Science Foundation Graduate Fellowship (T.R.A.), and Defense Advanced Research Projects Agency (T.R.A. and C.F.Q.).

6 December 1988; accepted 30 January 1989

Cnidocyte Mechanoreceptors Are Tuned to the Movements of Swimming Prey by Chemoreceptors

GLEN M. WATSON AND DAVID A. HESSINGER

Cnidocytes, the stinging cells of cnidarians, discharge nematocysts in response to physical contact accompanied by the stimulation of specific chemoreceptors. Cnidocytes in fishing tentacles of a sea anemone are now found to discharge nematocysts preferentially into targets vibrating at 30, 55, and 65 to 75 hertz. Moreover, in the presence of submicromolar concentrations of known chemosensitizers, such as N-acetylated sugars and mucin, these optima shift to 5, 15, 30, and 40 hertz, frequencies that correspond to the movements of swimming prey. Hence, chemoreceptors for these substances tune cnidocyte mechanoreceptors to frequencies that match the movements of the prey.

Cnidarians, such as hydra, jellyfish, corals, and sea anemones, rely primarily on chemical and mechanical perturbations in the environment to detect prey and predators because, in most cnidarians, vision is absent and photic detection is only crudely developed (*1*). Chemoreceptors are important in regulating prey capture (*2, 3*) and movement of the captured prey to the mouth (*4*). Cnidocytes (cnida-containing cells) discharge nematocysts and other cnidae [intracellular capsules containing eversible tubules (*5*)] into or onto the prey to capture it. This discharge involves a series of cellular (*6*) and mechanical processes that culminate in the rapid eversion of the tubule (*7*). Some everting tubules inject toxins into the prey, whereas others adhere to the surface of the prey or entangle its appendages (*8*).

Substances derived from prey are detected by at least two classes of chemoreceptors (*2*) that predispose cnidocytes to discharge cnidae in response to physical contact (*6*). One class of chemoreceptors is specific for free and conjugated N-acetylated sugars, and the other exhibits broad specificity for low molecular weight amino compounds (*2*). Receptors for N-acetylated sugars occur exclusively on supporting cells (*9*), cells that surround cnidocytes (Fig. 1). With one exception (*10*), the functional characteristics of specific mechanoreceptors in cnidarians have not been described. We now characterize the mechanoreceptors involved in triggering the discharge of nematocysts in the fishing tentacles of a sea anemone.

Monoclonal sea anemones (*Haliplanella luciae*) were reared under defined conditions (*11*) and fed a diet of brine shrimp nauplii (*Artemia salina*) (*12*). Experiments were performed approximately 72 hours after feeding. To test cnidocyte responsiveness, we touched the fishing tentacles with vibrating probes, each of which consisted of a 2-cm segment of monofilament, nylon fishing line having one end coated with a thin layer of gelatin (*11*). Microbasic p-mastigophore nematocysts discharged into the gelatin coating were counted (*11*). Vibrating probes have a flat frequency response from 5 to 100 Hz for displacements at the probe tip ranging from 35 to 700 μm (*13*). A probe

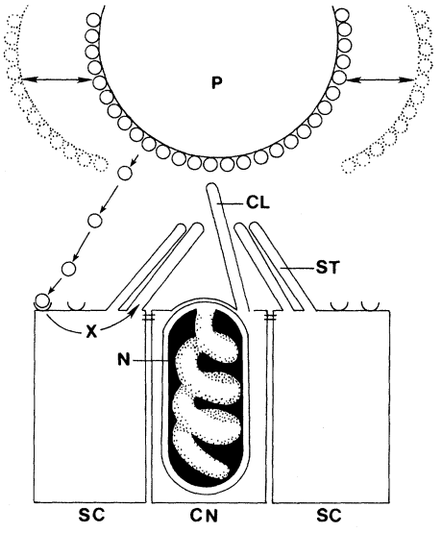

Fig. 1. Diagram of a cnidocyte–supporting cell complex. The cnidocyte (CN) contains a nematocyst (N). Supporting cells (SC) have receptors (curved lines at the top of each SC box) that detect N-acetylated sugars (○) (*9*) on or from prey (P). Receptor-ligand complexes initiate intracellular processes (**X**), which lengthen the stereocilia (ST) (*14*) and tune the cnidocyte mechanoreceptor to frequencies that match movements (double-headed arrows) produced by swimming prey. The mechanoreceptor consists of a single cilium (CL) originating from the cnidocyte and several stereocilia originating from the supporting cells (*20*).

Department of Physiology and Pharmacology, School of Medicine, Loma Linda University, Loma Linda, CA 92350.